IJMMM
International Journal of
Minerals, Metallurgy and Materials
矿物冶金与材料学报（英文版）

Characterization and properties of soft magnetic $(Fe_{0.5}Co_{0.5})_{75}B_{21}Nb_4$ metallic glasses subjected to cryogenic treatment and relaxation annealing

Zongqi Xiao, Xingyu Zhou, Xin Zhang, Qikun Huang, Li Cai, and Yan Wang

Cite this article as:

Zongqi Xiao, Xingyu Zhou, Xin Zhang, Qikun Huang, Li Cai, and Yan Wang, Characterization and properties of soft magnetic $(Fe_{0.5}Co_{0.5})_{75}B_{21}Nb_4$ metallic glasses subjected to cryogenic treatment and relaxation annealing, *Int. J. Miner. Metall. Mater.*, 32(2025), No. 8, pp. 1955-1964. https://doi.org/10.1007/s12613-024-3084-4

View the article online at SpringerLink or IJMMM Webpage.

INTERNATIONAL JOURNAL OF
Minerals, Metallurgy and Materials

Volume 32, Number 8, August 2025
Page 1955

Research Article https://doi.org/10.1007/s12613-024-3084-4

Characterization and properties of soft magnetic $(Fe_{0.5}Co_{0.5})_{75}B_{21}Nb_4$ metallic glasses subjected to cryogenic treatment and relaxation annealing

Zongqi Xiao[1)], *Xingyu Zhou*[1)], *Xin Zhang*[1)], *Qikun Huang*[2)], *Li Cai*[2)], *and Yan Wang*[1),✉]

1) School of Materials Science and Engineering, University of Jinan, Jinan 250022, China
2) Spintronics Institute, University of Jinan, Jinan 250022, China
(Received: 15 October 2024; revised: 31 December 2024; accepted: 31 December 2024)

Abstract: The effect of cryogenic treatment (CT) and relaxation annealing on the average nearest neighboring distance of atom (d_m), thermodynamic stability, soft magnetic properties, microhardness (H_v), and corrosion resistance of as-spun $(Fe_{0.5}Co_{0.5})_{75}B_{21}Nb_4$ metallic glasses (MGs) is studied. On the premise of maintaining a fully amorphous phase, appropriate CT and relaxation annealing are conducive to achieving the synergistic effect of increasing saturation magnetization (M_s) and reducing coercivity (H_c). Shallow CT at 213 K optimally enhances the soft magnetic properties of MGs. Given its low activation energy of nucleation and increased activation energy of growth, appropriate CT is beneficial for achieving uniform annealed nanocrystals in amorphous phases. The correlation between free volumes (FVs) and potential energy suggests that the variation in H_c depends on the expansion and contraction behavior of amorphous phases after different CT processes. The fitting formulas of H_c–d_m and M_s–H_v correlations demonstrate that soft magnetic parameters have a solid linear relationship with the contents of FVs and degree of dense random packing. Moreover, pitting resistance is improved by appropriate CT and relaxation annealing. This improvement is characterized by the promotion of the stability of the Nb-rich passive film formed during electrochemical corrosion in 3.5wt% NaCl solution.

Keywords: metallic glass; cryogenic treatment; relaxation annealing; soft-magnetic properties; corrosion resistance

1. Introduction

Since they were first discovered in the form of binary Au–Si alloy [1], metallic glasses (MGs) have attracted increasing attention owing to their superior properties over their crystalline counterparts [2–3]. Given their outstanding soft magnetic properties, such as high saturation magnetization (M_s), permeability, and electric resistance, and low coercivity (H_c) and core loss [4–6], Fe-based MGs have been applied as excellent soft magnetic materials in numerous electric and electronic fields [7].

In addition, the saturation magnetizations of Fe-based MGs and their nanocrystalline counterparts have approached those of silicon steels [8]. However, their wide industrial application is hindered by the processing complexity resulting from the high-heating-rate annealing to obtain nanograins and the existence of volatile phosphorus. An uncontrolled high annealing temperature caused the rapid grain growth and precipitation of the second phase, which sharply increased H_c (over 1000 times higher than the H_c of precursor materials) [9–10]. Crystallization-induced boundaries also degrade corrosion resistance performances [11]. Therefore, unremitting efforts are needed to develop novel and simple Fe-based MGs with a fully amorphous phase while achieving high glass-forming ability and excellent magnetic softness.

MGs have been observed to transform into novel metastable states after cryogenic treatment (CT) in liquid nitrogen, leading to irreversible changes in their main physical properties [12]. Combined with essential compositional design, CT enables effective modulation of soft magnetic properties in MGs while maintaining their fully amorphous structural integrity [13–14]. $[(Fe_{0.5}Co_{0.5})_{0.75}B_{0.2}Si_{0.05}]_{96}Nb_4$ MG with good soft magnetic properties and surprisingly high ductility was obtained through cryogenic thermal cycling (CTC) [15].

Furthermore, in consideration of the urgent requirement to extend the endurance life of magnetic components in various environments effectively, the development of excellent soft magnetic MGs with comprehensive performance, such as high corrosion resistance, has received considerable attention [16–18]. Accordingly, it is necessary to tailor MGs possessing excellent soft magnetic properties and high corrosion resistance.

Based on a simple compositional design, it is crucial to optimize the soft magnetic performance, mechanical properties, and corrosion resistance of MGs by modulating the atomic arrangement configuration of amorphous phase through CTs at different temperatures or relaxation annealing below the crystallization temperature. In the present study, appropriate relaxation annealing and CT were conduc-

✉ Corresponding author: Yan Wang E-mail: mse_wangy@ujn.edu.cn

Springer

ted on as-spun $(Fe_{0.5}Co_{0.5})_{75}B_{21}Nb_4$ MG ribbons with quaternary constituents. The microstructures, thermal stability, soft magnetic properties, microhardness, and corrosion resistance of these MG ribbons in 3.5wt% NaCl solution were explored in detail.

2. Experimental

2.1. Preparation and processing of MG ribbons

Alloy ingots with a nominal component of $(Fe_{0.5}Co_{0.5})_{75}B_{21}Nb_4$ were prepared by arc-melting a mixture of the raw materials Co, Nb, and B with purity above 99.95wt% and pre-alloys of Fe–B (>99wt% purity) in a Ti-gettered high-purity Ar atmosphere. The MG ribbons were fabricated via melt spinning under vacuum conditions, utilizing a Cu wheel rotating at 3400 r·min^{-1} (linear velocity of approximately 30 m·s^{-1}) in vacuum. The width and thickness of the obtained ribbons were approximately 2–2.5 mm and 20–23 μm, respectively.

The as-spun ribbons were subjected to relaxation annealing at 740 K (below the onset crystallization temperature, T_{x1} = 755 K) in a vacuum tube furnace, with a holding time of 600 s. In addition, the as-spun ribbons were cryogenically treated at 77 K (deep CT), 173 K (moderate CT), and 213 K and 253 K (shallow CT) for 12 h by using a thermostatic reaction bath (DLSB ZLD-120C, Blue Power, China) with ethanol as a medium. The corresponding samples are denoted as shown in Table 1.

Table 1. Designation of the tested $(Fe_{0.5}Co_{0.5})_{75}B_{21}Nb_4$ MGs under different treatment temperature conditions

Treatment condition	77 K	173 K	213 K	253 K	As-spun	740 K
Designation	Sc77	Sc173	Sc213	Sc253	Sspun	Sa740

2.2. Characterization

The microstructures of the tested MG ribbons were examined through X-ray diffraction (XRD, D8 Advance, Bruker, German) using Cu-K$_\alpha$ radiation (λ = 0.15406 nm). Thermal stability was analyzed by employing differential scanning calorimetry (DSC, TGA/DSC1, Mettler-Toledo, USA) at a heating rate of 10–40 K·min^{-1} under a continuous flow of purified Ar. M_s and H_c were measured by a vibrational sample magnometer (VSM, LakeShore7404, Lake Shore, USA) at room temperature (approximately 298K) with a maximum applied field of ±10000 Oe. All samples for hysteresis loop measurements had the same dimensions of approximately 2 mm long and 2 mm wide to avoid the effects of ribbon geometry. The Vickers' microhardness on the wheel-side ribbon was measured by using a microhardness tester (HVS-1000ZT, Feng Zhi, China) with a loading force of 500 N and a holding time of 15 s. The obtained microhardness values were the average of more than 10 indentations for each sample.

Corrosion behavior was evaluated through electrochemical polarization measurement in 3.5wt% NaCl aqueous solution by using an electrochemical workstation (CHI660E, Chenhua, China). The potential of cathodic polarization scans ranged from −2 to 0.5 V with a sweep rate of 2.0 mV·s^{-1}. The three-electrode cell included a platinum counter electrode and an Ag/AgCl reference electrode. The wheel-side ribbon was used as the working electrode with an average immersed area of 0.2 cm^2. Before the acquisition of polarization curves, all samples were immersed in the 3.5wt% NaCl aqueous solution and underwent open circuit potential testing for approximately 600 s until a stable trend was obtained.

The surface corrosion morphologies of the tested ribbons were observed by using field-emission scanning electron microscopy (FESEM, QUANTA FEG 250, FEI, USA).

3. Results and discussion

3.1. Structural characterization

Fig. 1 provides the XRD results of the MG ribbons after relaxation annealing and CT under different temperature conditions. It shows that the XRD pattern of each tested sample mainly contains a broad diffuse peak, representing the formation of a typical amorphous phase (Fig. 1(a)). Optical photos

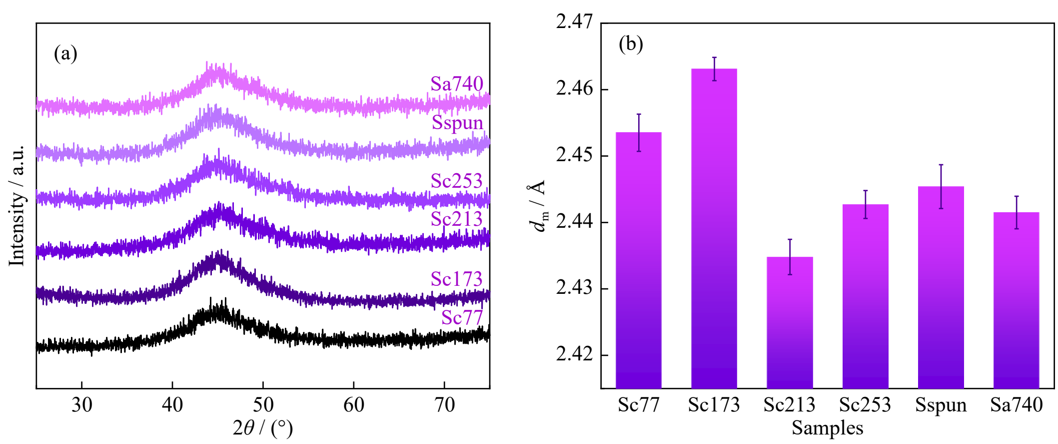

Fig. 1. XRD patterns (a) and d_m variation (b) of the $(Fe_{0.5}Co_{0.5})_{75}B_{21}Nb_4$ MG ribbons under different treatment temperature conditions.

(Fig. S1, see the Supplementary Information) reveal that after bending at 180° or multiple bending cycles, the CT MG ribbons clearly show preserved continuity. Although the MG ribbons have good plasticity, they cannot withstand severe bending. Therefore, this finding demonstrates that appropriate CT is the preferred treatment for improving soft magnetic properties and maintaining amorphous plasticity.

The average nearest neighboring distance of atoms (d_m) in the MGs is an accessible index for assessing atomic topological short-range ordering and stability [19]. Such an index could provide rudimentary insight into possible structural relaxation or atomic rearrangement. The parameter d_m is inferred from Eq. (1):

$$2d_m\sin\theta = 1.23\lambda \tag{1}$$

where λ is the wavelength of Cu-K_α radiation; θ is the diffraction peak position (determined by fitting the main peak by the Gaussian profile); and 1.23 is the correction factor applicable for liquid and amorphous solids [20]. Fig. 1(b) shows that the d_m values of the Sa740, Sc253, and Sc213 ribbons are lower than that of Sspun. In particular, among the ribbons, the Sc213 ribbon shows the greatest reduction in d_m. This finding also indicates that shallow CT and relaxation annealing induce the contraction of average distance and dense atomic packing. Dokukin *et al*. [13] reported that the interatomic distance of $Fe_{78}Cu_1Nb_4B_{3.5}Si_{13.5}$ MG ribbons showed reduction under CT at 77.8 K.

However, under moderate CT (173 K) and deep CT (77 K) conditions, d_m exhibits a considerable increase, revealing the reconfiguration of a loose amorphous structure. This increase is more pronounced in Sc173 than in other ribbons. Fig. 2 is a comprehensive illustration of the thermodynamic behaviors of the MGs treated at the heating rate of 20 K·min^{-1}. Fig. 2(a) shows the presence of three clearly observable exothermic peaks at approximately 790 and 840–900 K, further confirming the amorphous characteristics of all the MG ribbons. The variation trends of T_{x1} and crystallization peak temperature (T_{p1}) obtained from the first exothermic peak are presented in Fig. 2(b). Notably, the shallow and deep CT result in lower T_{x1} and T_{p1} values compared to relaxation annealing, demonstrating reduced thermal stability of the MGs.

3.2. Thermal stability and crystallization behaviors

The crystallization activation energies of Sspun, Sc213, and Sc77 are selected for measurement to qualitatively assess the effect of CT on the thermal stability of the tested MGs. The DSC curves of the three samples treated at the heating rates of 10, 20, 30, and 40 K·min^{-1} are plotted in Fig. 3. The related thermodynamic events are found to invariably move toward high temperatures with increasing heating rates.

In accordance with the exothermic peak shifts at different heating rates, the effective crystallization activation energies associated with nucleation ($E_{T_{x1}}$) and growth ($E_{T_{p1}}$) are evaluated by using the Kissinger method and depicted by Eq. (2) [21]:

$$\ln\frac{T^2}{\beta} = \frac{E}{RT} + C \tag{2}$$

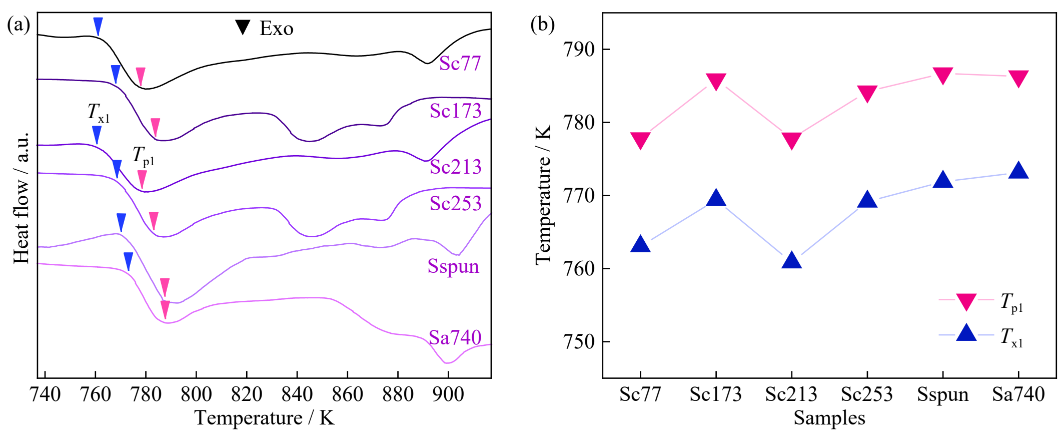

Fig. 2. DSC curves (a) and variation trends of T_{x1} and T_{p1} (b) of all the tested MGs acquired at a heating rate of 20 K·min^{-1}.

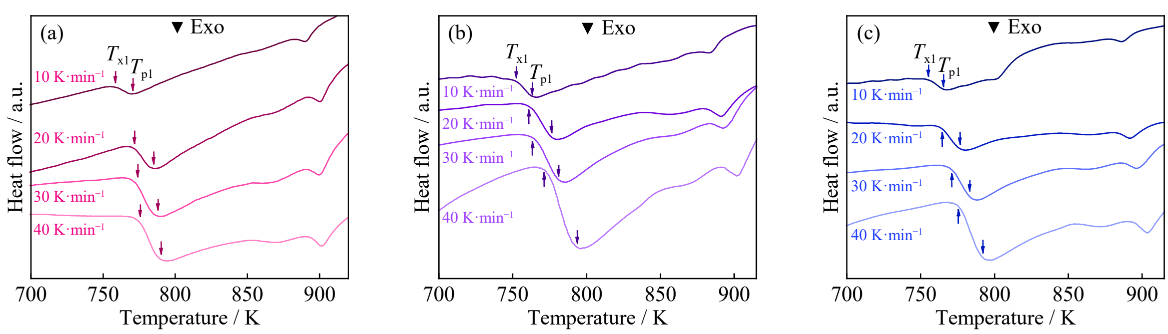

Fig. 3. DSC curves of the Sspun (a), Sc213 (b), and Sc77 (c) MGs obtained at different heating rates.

where C is the temperature-independent constant, T is the specific temperature (T_{x1} and T_{p1} herein), β is the heating rate, R is the gas constant of 8.314 J·K^{-1}·mol^{-1}, and E is the corresponding apparent activation energy. In the present study, the values of $E_{T_{x1}}$ and $E_{T_{p1}}$ are deduced from T_{x1} and T_{p1}, which are associated with nucleation and growth, respectively.

Herein, $E_{T_{x1}}$ and $E_{T_{p1}}$ are determined from the slope of the plot of $\ln(T^2/\beta)$ as a function of 1000/T, as illustrated in Fig. 4 and plotted in Fig. 5. All the Kissinger plots of $E_{T_{x1}}$ (Fig. 4(a)–(c)) and $E_{T_{p1}}$ (Fig. 4(d)–(f)) exhibit a strong linear relationship, with data points showing good distribution alongside the fitting line. Notably, the three MGs show $E_{T_{x1}}$ values that remarkably surpass $E_{T_{p1}}$, suggesting that nucleation is substantially more difficult than grain growth in the main crystallization process. The $E_{T_{x1}}$ values of Sc77 and Sc213 are 333.7 and 337.2 kJ·mol^{-1}, respectively, which are 12.8% and 11.8% lower than that of Sspun (382.5 kJ·mol^{-1}), respectively. This finding indicates that compared with the Sspun sample, the CT samples require a lower energy barrier for the primary crystallization nucleation of their amorphous phases [22]. However, the $E_{T_{p1}}$ values of the MGs subjected to CT are 16.1% and 10.7% higher than that of Sspun. Notably, CT is beneficial for the nucleation of the $(Fe_{0.5}Co_{0.5})_{75}B_{21}Nb_4$ amorphous phase and inhibits grain growth behavior. This effect demonstrates that through appropriate CT, the amorphous phase easily generates uniform annealed nanocrystals.

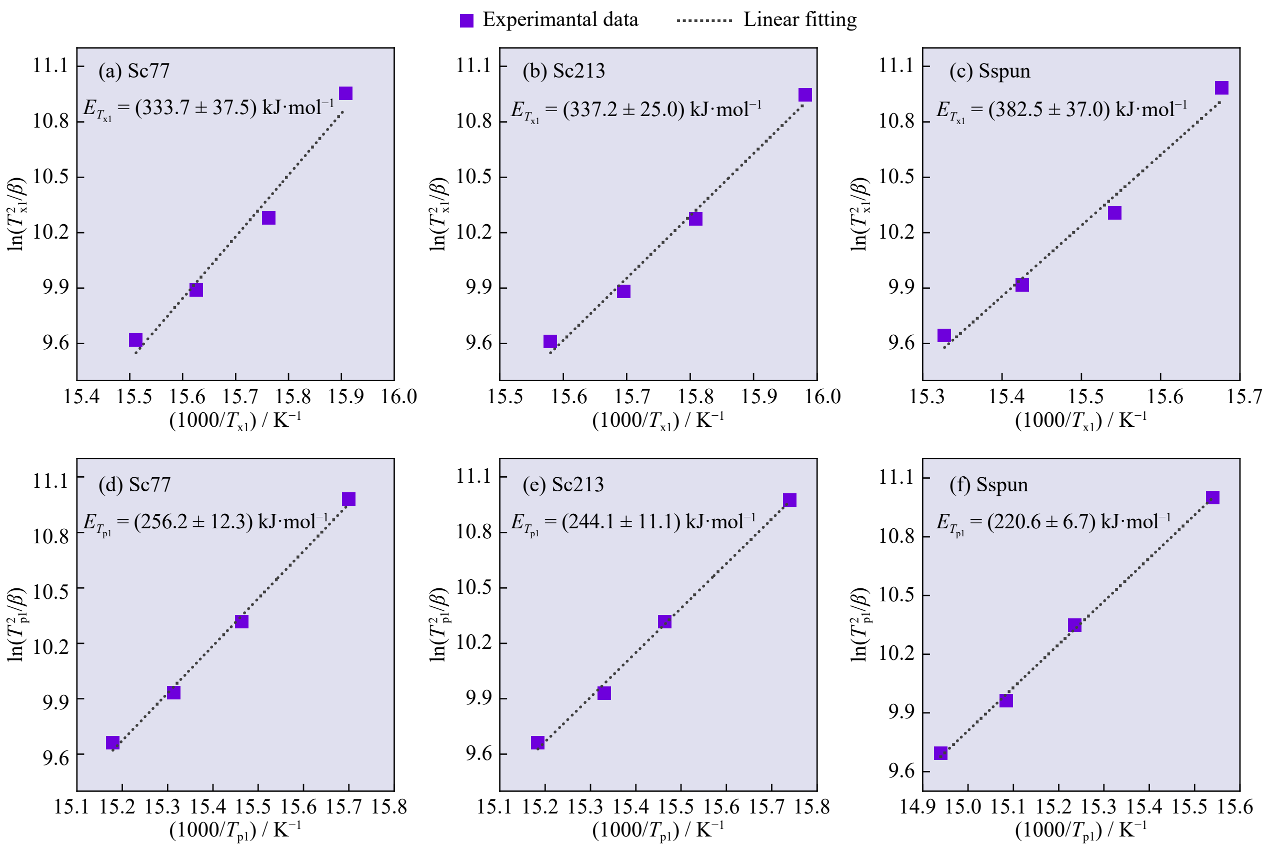

Fig. 4. Kissinger plots ($\ln(T^2/\beta)$ vs. 1000/T) and the corresponding $E_{T_{x1}}$ and $E_{T_{p1}}$ for Sc77 (a, d), Sc213 (b, e), and Sspun (c, f) MGs.

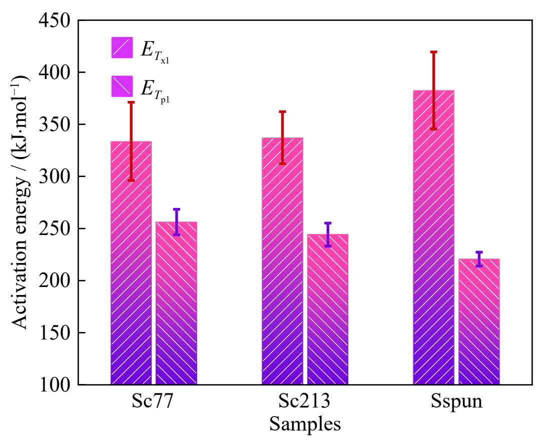

Fig. 5. Variation trends of the $E_{T_{x1}}$ and $E_{T_{p1}}$ values of the Sc77, Sc213, and Sspun MGs.

3.3. Correlation between soft magnetic properties and structures

Fig. 6(a) shows the magnetic hysteresis loops of the tested MGs and the zoomed-in view of the central part of the curves, where vertical coordinate is the mass magnetization (M) of samples and horizontal coordinate is the applied field (H). The H_c values of all the tested samples are invariably below 1.8 Oe, and their loop silhouettes are similarly elongated, proving typically soft magnetic characteristics.

Fig. 6(b) displays that CT and relaxation annealing are conducive to increasing the M_s values of the tested MGs, with CT having a more optimal effect than relaxation annealing. This finding shows that the sample subjected to annealing-induced relaxation has a modest improvement of 5.2% in M_s

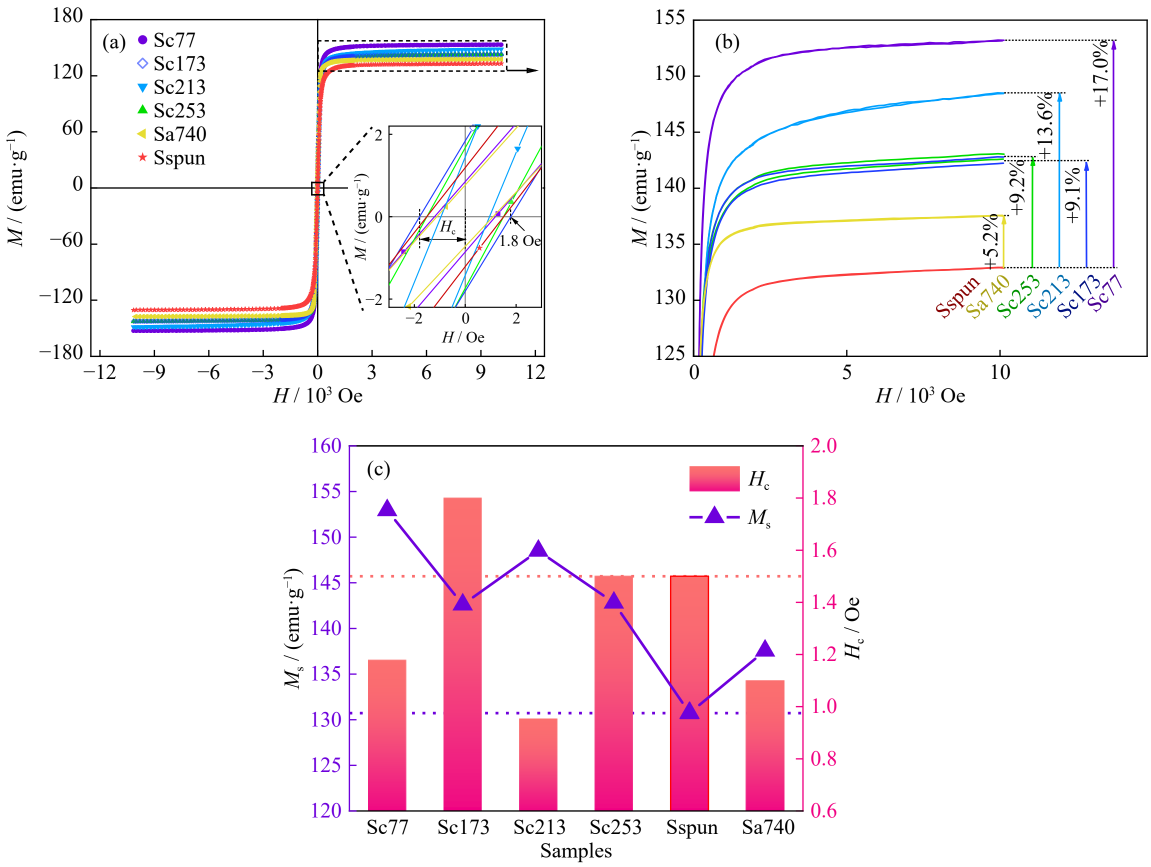

Fig. 6. Magnetic hysteresis loops and inset showing a zoomed-in view of the central part of the curve (a), loop ends showing the change in the magnitude of M_s (b), and variations in the H_c and M_s (c) of the $(Fe_{0.5}Co_{0.5})_{75}B_{21}Nb_4$ MGs subjected to different treatment temperatures.

over the Sspun. However, reducing the CT temperature does not have a monotonically linear effect on improving the M_s values of the MGs. Instead, the optimal CT temperature is 77 K, followed by 213 K. These temperatures exhibit increases of 17.0% and 13.6%, respectively, compared to the Sspun state.

CT leads to irreversible atom redistribution, promoting the densification of the cluster structure in the amorphous matrix [13]. Moreover, structural relaxation in the MGs was usually accompanied by a minor volume contraction resulting from the recombination/annihilation of high- and low-density regions in the glassy phase or liquid-like sites [23]. Accordingly, the volume contraction of the MGs may enhance the exchange interaction between magnetic atoms, resulting in an increase in M_s. Therefore, this situation demonstrates that the contracted cluster structure of MG ribbons after CT is beneficial for improving M_s. However, in this study, M_s does not increase linearly with decreasing cryogenic temperature. This finding suggests that the amorphous structure in the $(Fe_{0.5}Co_{0.5})_{75}B_{21}Nb_4$ MG may exhibit contraction and abnormal anti-inflation behavior during CT. Below, the evolution behavior of cluster structures in the MGs is further elaborated upon in conjunction with the H_c values under CT.

Fig. 6(c) illustrates that except for the Sc173 and Sc253 ribbons, Sc77, Sc213, and Sa740 possess low H_c values of 1.2, 0.95, and 1.1 Oe, respectively, which are 20%, 37%, and 27% lower than that of the Sspun MG, respectively. Therefore, these findings reveal that appropriate CT promotes the improved magnetic softness of the MGs.

The above results demonstrate that we have optimized soft magnetic performance while maintaining the completely amorphous phase of the $(Fe_{0.5}Co_{0.5})_{75}B_{21}Nb_4$ MGs. The synergistic effect of increasing M_s and reducing H_c has been achieved through commonly used processing methods, including appropriate relaxation annealing and CT. An overall comparison reveals that appropriate shallow CT at 213 K optimizes the above synergistic effect to the greatest extent.

The dispersed free volumes (FVs) generated during rapid solidification in the MGs agglomerate to form quasi-dislocation dipoles [24], which serve as pinning centers for magnetic domain walls [8,25–26]. Hence, the contribution of FVs to H_c, as shown in the following Eq. (3), must be considered:

$$H_c = P(F, L_{\mathrm{DW}})\sqrt{\Delta\rho}\frac{\lambda_s}{J_s} \tag{3}$$

where $P(F, L_{\mathrm{DW}})$ is a constant including the domain wall area (F) and domain width (L_{DW}), $\Delta\rho$ is the amount of excess free volume, λ_s is the saturation magnetostriction, and J_s is the saturation polarization. Accordingly, the decrease in excess FVs could induce lower H_c. With the occurrence of structural relaxation during the initial annealing, residual stress and defects, such as FVs, are reduced or annihilated; this effect alleviates magnetic anisotropy and leads to increased M_s and decreased H_c [7]. This phenomenon accounts for the improvement in the soft magnetic performance of Sa740.

Fig. 7(a) schematically illustrates the variational behavior of FVs in the amorphous matrix after different CT processes. The MG exhibited significantly enhanced H_c, which was primarily attributed to the synergistic effects of intensified residual stresses and FV concentration induced by rapid solidification during the melt-spinning process [7]. In the sample subjected to shallow CT at 253 K, the contraction of the amorphous matrix and its FVs are negligible, and the potential energy does not markedly reduce. Decreasing the CT temperature to 213 K accelerates the contraction of MGs. This effect is accompanied by the annihilation or reduction of FVs. Lan *et al*. [27] found that MGs contain structural building blocks with intermediate length scales (extending to the order of tens of angstroms) that connect amorphous and crystalline states. Therefore, the amorphous structure with this configuration tends to contract easily under appropriate external conditions. Moreover, CT caused the short-range order change of the Fe-based MGs, inducing a new metastable equilibrium state, which was stable after CT finishing [12]. Qiao group [28] reported that CTC treatment induced different activation volumes of bulk metallic glass (BMG). Fig. 7(b) implies that the Sc213 structure becomes increasingly homogeneous and acquires relatively low potential energy, exhibiting low H_c.

However, under moderate CT at 173 K, the amorphous structure reaches the threshold of contraction and instead exhibits abnormal anticontraction behavior, showing an increase in the size or quantity of FVs. The corresponding potential energy tends to increase, displaying the enhancement in H_c. In deep CT, the potential energy may cross the potential barrier and decrease. These phenomena are accompanied by a reduction in the number of FVs and a corresponding decrease in H_c.

In this study, the variation trends of d_m and H_c are explored to obtain an improved understanding of the dependency relationship between H_c and amorphous structures. The linear relation between these two parameters is described in Fig. 8 on the basis of our previous work on soft magnetic FeCo-based MG ribbons [29–31]. Herein, the correlation model of d_m and H_c is proposed to construct preliminarily the dependency relationship between amorphous structures and soft magnetic performance. Given the diverse fabrication parameters and characterization means for the three types of FeCo-based MG ribbon systems, the H_c values span different orders of magnitude.

In consideration of the monotonic linear relationship between H_c and d_m, the feasible formula models are obtained by using the linear fitting method, as shown in Eqs. (4)–(6).

$$H_c = 22.8d_m - 54.5 \tag{4}$$

$$H_c = 4.3d_m - 9.6 \tag{5}$$

$$H_c = 0.96d_m - 2.2 \tag{6}$$

A series of tests reveal that the calculated slope values range from 0.96 to 22.8 (10^{-1} to 10^1), while intercept values span from 2.2 to 54.5 (10^0 to 10^1), covering distinct orders of magnitude. The broad ranges of these parameters can be related to factors such as the Fe/Co atomic ratio, dopant elements, and apparatus error parameters.

Despite the standard error of the above indices, the results are sufficiently robust such that the variation trends of the correlation of H_c and d_m within groups are invariably positive. This situation implies that the low average neighboring distance of atoms is associated with the improved magnetic softness of the FeCo-based MG ribbons. For example, high d_m values may be indicative of low symmetric clusters and, therefore, long fluctuation correlation lengths, from which high coercive fields of relaxation originate [32]. Therefore, the changes in d_m and structure-sensitive H_c among various energy states are highly in sync despite the nonmonotonic trend of these values and treatment temperatures.

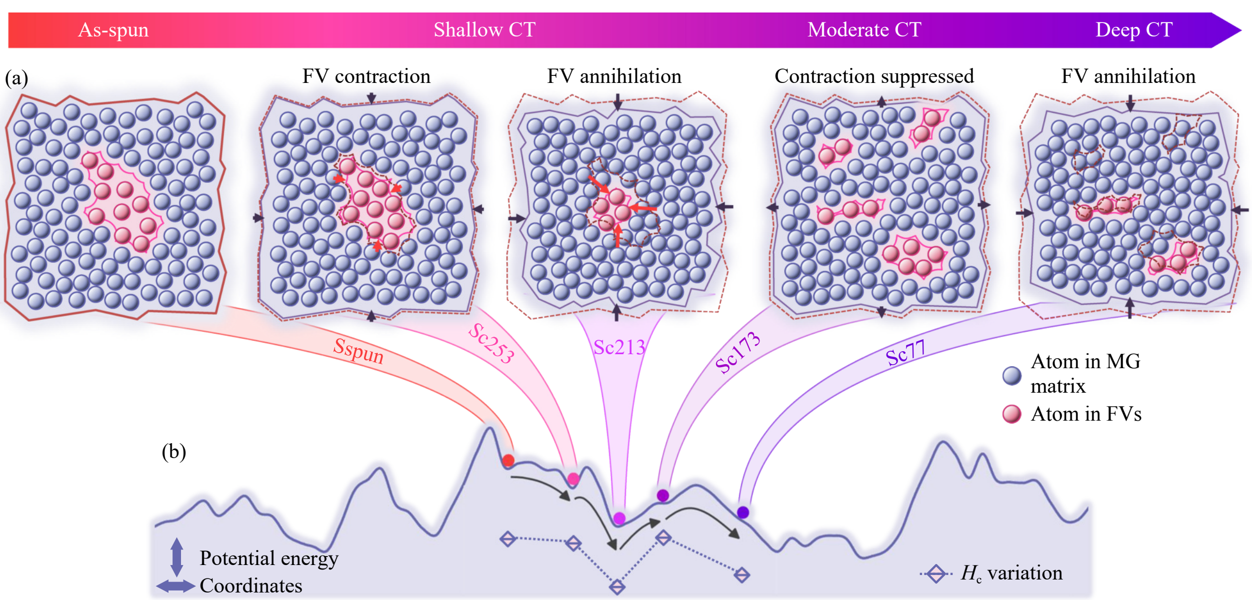

Fig. 7. Schematic of the variational behavior of FVs in the amorphous matrix (a) and the corresponding changes in H_c and potential energy landscape (b) after different CT processes.

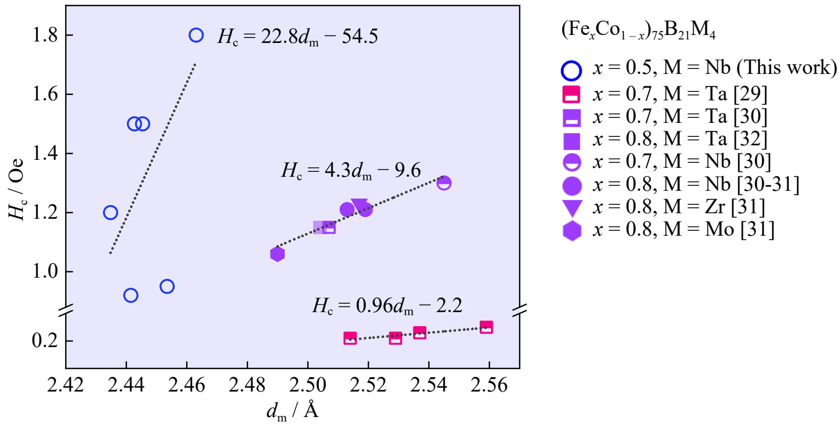

Fig. 8. Variation in H_c as a function of the d_m values of the MGs tested in the present work together with those of $(Fe_xCo_{1-x})_{75}B_{21}M_4$ MGs in previous studies.

3.4. Vicker's microhardness

The microhardness data on the wheel-side surface of the MG ribbons are plotted in Fig. 9. The Sspun sample exhibits the lowest microhardness of HV 788. The cryogenic treated and as-annealed ribbons all show higher microhardness than the Sspun sample. Among the samples, Sc77 has the highest microhardness of HV 854, which is 8.4% higher than that of Sspun. The increased microhardness of the Fe–Co–Ni–Cr–Mo–C–B–Y BMG has been attributed to the decreased FVs in alloys [33]. Moreover, the high microhardness of the $Co_{40}Fe_{22}Ta_8B_{30}$ MG could be explained by the high degree of dense random packing, as confirmed by the high average co-ordination number of the first coordination shell and very high thermal stability [34].

Moreover, a linear correlation is observed between M_s and Vicker's microhardness. Accordingly, the variation in M_s as a function of the microhardness (H_v) of the tested MGs is described in Fig. 10. In contrast to microhardness, M_s follows an approximately positive trend. The model that fits this trend is described by Eq. (7):

$$M_s = 0.35H_v - 141.98 \tag{7}$$

The present study reveals that M_s can be roughly determined by the change in MG ribbon microhardness. As mentioned above, the appropriate relaxation annealing and CT have a significant influence on the contents of free volume and degree of dense random packing, thus exerting a positive impact on the magnetic characteristic parameters of the treated $(Fe_{0.5}Co_{0.5})_{75}B_{21}Nb_4$ MGs. However, since these patterns are derived from a limited dataset in our studies, more extensive testing and analysis are required to establish statistically robust rules.

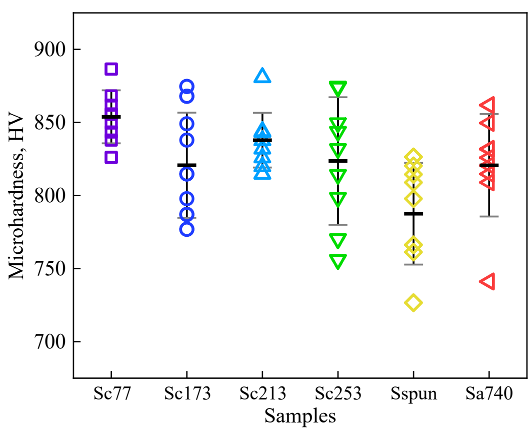

Fig. 9. Microhardness on the wheel-side surface of the $(Fe_{0.5}Co_{0.5})_{75}B_{21}Nb_4$ MGs under different treatment temperature conditions.

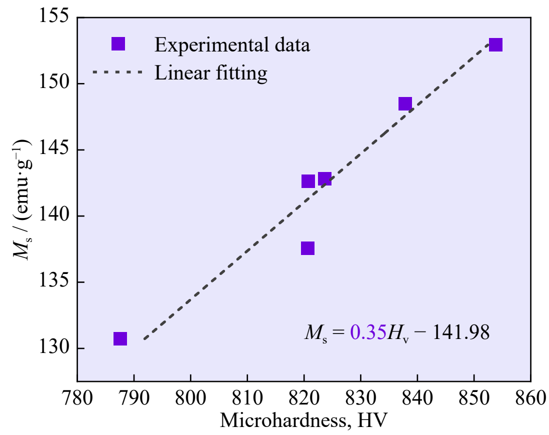

Fig. 10. Variation in M_s as a function of the microhardness of the $(Fe_{0.5}Co_{0.5})_{75}B_{21}Nb_4$ MGs subjected to different treatments.

3.5. Corrosion resistance and passivation behaviors

The Sc173, Sspun, and Sa740 MGs are subjected to an electrochemical corrosion test in 3.5wt% NaCl solution, as shown in Fig. 11, to explore the effect of CT and relaxation annealing on the corrosion resistance of the MG ribbons. Potentiodynamic polarization curves illustrate that the tested samples all experience anodic activation and pitting corrosion with a wide passivation zone (Fig. 11(a)).

The corrosion potential (E_{corr}), corrosion current density (i_{corr}), and passive region width ($\Delta E_P = E_{pit} - E_{corr}$, where E_{pit} represents the pitting corrosion potential) are selected to evaluate comprehensive corrosion resistance, as displayed in Fig. 11(b). Sa740 has more positive E_{corr} (−1.302 V) but higher i_{corr} (2.252 μA·mm^{-2}) than Sspun. This result indicates that although relaxation annealing contributes to the difficulty of anodic activation, its rate accelerates once corrosion occurs.

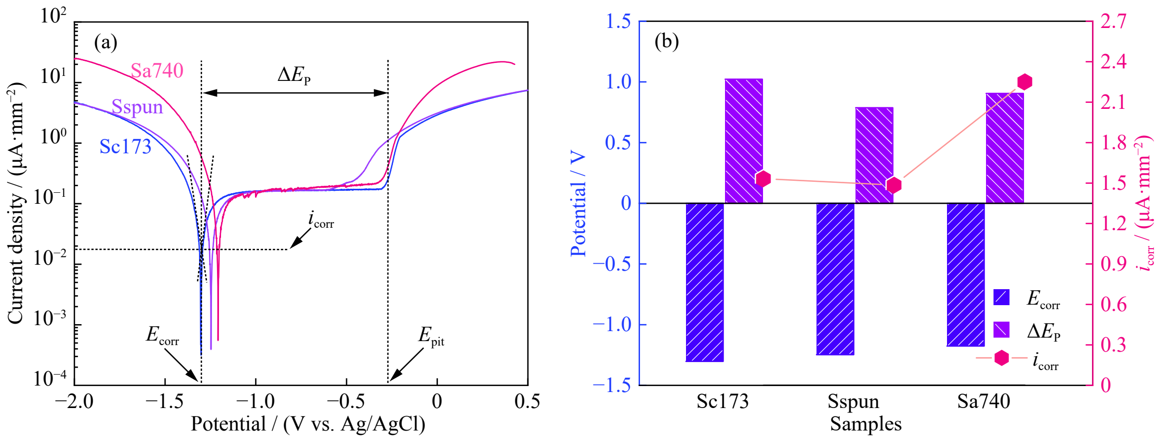

Fig. 11. Potentiodynamic polarization curves (a) and variation in the E_{corr}, i_{corr}, and ΔE_P (b) of the Sc173, Sspun, and Sa740 MG ribbons.

Similarly, CT at 173 K weakens the general corrosion resistance of the MGs. The ability of a material to resist localized attack on its passive film is a function of its ΔE_P. The ΔE_P values of Sc173 and Sa740 are larger than those of Sspun, where Sc173 shows optimal ΔE_P (up to 1.022 V) in 3.5wt% NaCl solution. Appropriate CT and relaxation annealing improve pitting resistance by promoting the stability of the passive film formed during electrochemical corrosion. Corrosion surface morphology and element distribution analyses are conducted to explore corrosion characteristics further.

The corrosion morphologies of Sspun and Sc173 after the potentiodynamic polarization test are investigated through FESEM, as shown in Figs. 12 and 13, respectively. The passive film on the Sspun surface exhibits pronounced orthogonal cracking patterns, demonstrating characteristic mud-crack morphology (Fig. 12(a)). Additionally, a large amount of fragmented corrosion products with sizes of approximately 1–2 μm are densely distributed on the film surface, as shown in Fig. 12(b). The zoomed-in view of the passive film in Fig. 12(c) indicates that the film is composed of dense nanolayered products. The elemental mappings corresponding to Fig. 12(d)–(h) shows that the corrosion products are enriched in oxygen, and the Nb element is prominent in the passive film.

B, Fe, and Co elements exhibit a uniform distribution in the passive film of Sc173. Although some cracked passive films have peeled off, the corrosion surface of Sc173 MG is relatively flat without observable bulging, as shown in Fig. 13(a). Corrosion products with two different particle sizes (approximately 1 and 4 μm) are distributed on the surface of the passive film (Fig. 13(b)), while similar to that of Sspun, the passive film of Sc173 is composed of dense nanosheets (Fig. 13(c)). As clearly shown in Fig. 13(d)–(h), Fe and Co are enriched in the smooth inner surface (Region I), while the passive film (Region II) of Sc173 is clearly enriched in Nb and O elements. This result demonstrates that Nb is the key element promoting the formation of passive films [35–37]. The formed Nb-rich passive film effectively protects the Fe- and Co-rich fresh surface. The addition of Nb into the Cu–Zr–Al–Nb MGs effectively promoted the passivation of the alloys by reducing the active current peak and passive current density [38].

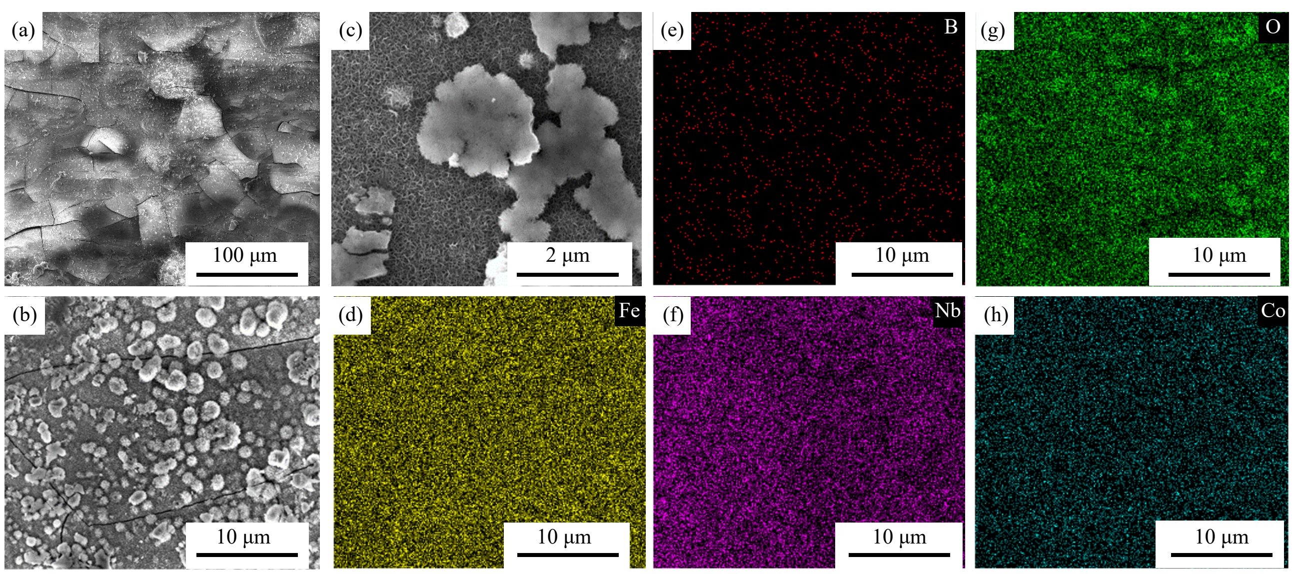

Fig. 12. FESEM images of the corroded Sspun surface after electrochemical testing in 3.5wt% NaCl solution (a–c) and the elemental mappings (d–h) corresponding to (b).

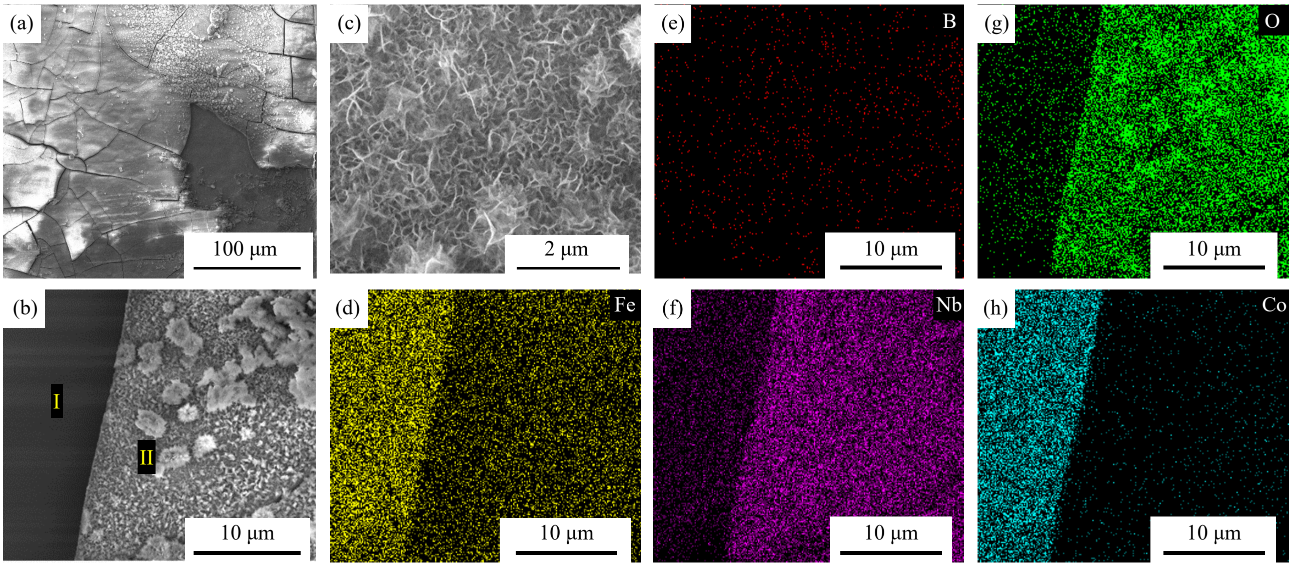

Fig. 13. FESEM images of the corroded Sc173 surface after electrochemical testing in 3.5wt% NaCl solution (a–c) and the elemental mappings (d–h) corresponding to (b).

Existing studies have demonstrated that a large number of vacancies were significantly inhibited from condensing to form voids in the liquid-like structure at the reaction surface. This condition manifests as the minimalized tendency of pit initiation and passive film rupture [39–40]. CT is speculated to further suppress the mobility of vacancies and synergistically suppress point defects and vacancy condensation on the reaction surface with Nb atoms. Passivation films are consequently less prone to rupture, explaining the overall enhancement in pitting resistance.

4. Conclusions

CT and relaxation annealing are utilized to induce the local atomic rearrangement of the $(Fe_{0.5}Co_{0.5})_{75}B_{21}Nb_4$ MG ribbons, thereby modulating their thermodynamic stability, soft magnetic properties, microhardness, and corrosion resistance in 3.5wt% NaCl solution. The results of this work are summarized as follows:

(1) The calculated crystallization activation energies show that CT is beneficial for crystallization nucleation and enhances the inhibition of grain growth behavior, facilitating the formation of uniform annealed nanocrystals in the amorphous phase.

(2) Compared with relaxation annealing, CT has a more optimal effect on increasing the M_s values of MGs. Deep CT (77 K) and shallow CT (213 K) increase M_s by 17.0% and 13.6%, respectively. Moreover, the Sc77, Sc213, and Sa740 MGs exhibit lower H_c values of 1.2, 0.95, and 1.1 Oe, respectively, compared to the Sspun MG. Among the tested MGs, Sc213 subjected to shallow CT displays the optimal synergy of M_s and H_c.

(3) A schematic model concerning the variational correlation among the amorphous matrix, FV, and potential energy is proposed on the basis of the speculated amorphous microstructural evolution after shallow/moderate/deep CT. It demonstrates that the moderate CT of MGs induces abnormal anticontraction behavior, resulting in an increase in the size or quantity of FVs and a corresponding enhancement in H_c.

(4) The obtained fitting formulas of H_c–d_m and M_s–H_v correlations demonstrate that soft magnetic parameters have a solid linear relationship with the contents of free volume and degree of dense random packing.

(5) Appropriate CT and relaxation annealing improve pitting resistance by promoting the stability of the Nb-rich passive film that forms during electrochemical corrosion.

Acknowledgements

The authors acknowledge financial support from the National Natural Science Foundation of China (No. 52271146), New 20 Items of Colleges and Universities in Jinan, China (No. 202228111), and University of Jinan Disciplinary Cross-Convergence Construction Project 2023, China (No. XKJC-202311).

Conflict of Interest

The authors declare that they have no known competing financial interests or personal relationships that could have appeared to influence the work reported in this paper.

Supplementary Information

The online version contains supplementary material available at https://doi.org/10.1007/s12613-024-3084-4.

References

[1] W. Klement, R.H. Willens, and P. Duwez, Non-crystalline structure in solidified gold-silicon alloys, *Nature*, 187(1960), No. 4740, p. 869.

[2] H. Zohdi, M. Bozorg, R. Arabi Jeshvaghani, H.R. Shahverdi, and S.M.M. Hadavi, Corrosion performance and metal ion re-

lease of amorphous and nanocrystalline Fe-based alloys under simulated body fluid conditions, *Mater. Lett.*, 94(2013), p. 193.

[3] H.H. Hsieh, W. Kai, R.T. Huang, C.Y. Lin, and T.S. Chin, Air oxidation of an $Fe_{72}B_{22}Y_6$ bulk amorphous alloy at 600–700°C, *Intermetallics*, 14(2006), No. 8-9, p. 917.

[4] F.J. Liu, T. Zhang, S.J. Pang, and K.F. Yao, Ductile Fe-based amorphous alloys with high iron content, *Int. J. Miner. Metall. Mater.*, 17(2010), No. 2, p. 199.

[5] D.A. Milkova, A.I. Bazlov, E.N. Zanaeva, *et al.*, (Fe–Ni)-based glassy alloy containing Nb and Cu with excellent soft magnetic properties, *J. Non-Cryst. Solids*, 609(2023), art. No. 122234.

[6] F. Wang, A. Inoue, Y. Han, *et al.*, Soft magnetic Fe–Co-based amorphous alloys with extremely high saturation magnetization exceeding 1.9 T and low coercivity of 2 A/m, *J. Alloy. Compd.*, 723(2017), p. 376.

[7] H.X. Li, Z.C. Lu, S.L. Wang, Y. Wu, and Z.P. Lu, Fe-based bulk metallic glasses: Glass formation, fabrication, properties and applications, *Prog. Mater. Sci.*, 103(2019), p. 235.

[8] X.S. Li, J. Zhou, L.Q. Shen, B.A. Sun, H.Y. Bai, and W.H. Wang, Exceptionally high saturation magnetic flux density and ultralow coercivity via an amorphous–nanocrystalline transitional microstructure in an FeCo-based alloy, *Adv. Mater.*, 35(2023), No. 50, art. No. 2205863.

[9] Z.G. Zheng, Y.B. Chen, J. Wei, X. Wang, Z.G. Qiu, and D.C. Zeng, Enhanced M_s of Fe-rich Fe–B–Cu amorphous/nanocrystalline alloys achieved by annealing treatments, *J. Alloy. Compd.*, 939(2023), art. No. 168621.

[10] X.L. Zhang, Y. Wu, R.R. Liu, J.H. Liu, and H.T. Zhou, A study of crystallization behavior and magnetic property of Co-based alloy, *J. Non-Cryst. Solids*, 619(2023), art. No. 122562.

[11] F.X. Qin, H.F. Zhang, Y.F. Deng, B.Z. Ding, and Z.Q. Hu, Corrosion resistance of Zr-based bulk amorphous alloys containing Pd, *J. Alloy. Compd.*, 375(2004), No. 1-2, p. 318.

[12] S.G. Zaichenko, N.S. Perov, A.M. Glezer, *et al.*, Low-temperature irreversible structural relaxation of amorphous metallic alloys, *J. Magn. Magn. Mater.*, 215(2000), p. 297.

[13] M.E. Dokukin, N.S. Perov, E.B. Dokukin, A.I. Beskrovnyi, and S.G. Zaichenko, Changes in the short-range order and magnetic properties of the amorphous magnetic metal alloy $Fe_{78}Cu_1Nb_4B_{3.5}Si_{13.5}$ following cryogenic treatment, *Physica B*, 368(2005), No. 1-4, p. 267.

[14] Y. Meng, Y.G. Wang, L. Zhu, C.C. Cao, and Y.D. Dai, Effect of thermal cycling treatment on local structure, thermal stability and magnetic properties of $Fe_{80}Si_{8.75}B_{10}Cu_{1.25}$ metallic glass, *J. Non-Cryst. Solids*, 471(2017), p. 406.

[15] S.Y. Di, J. Zhou, M.J. Cai, *et al.*, Improved ductility of annealed Fe-based metallic glass with good soft magnetic property by cryogenic thermal cycling, *J. Alloy. Compd.*, 960(2023), art. No. 170686.

[16] X.Y. Peng, Y.H. Tang, X.B. Ding, *et al.*, Fe-based amorphous coating prepared using high-velocity oxygen fuel and its corrosion behavior in static lead-bismuth eutectic alloy, *Int. J. Miner. Metall. Mater.*, 29(2022), No. 11, p. 2032.

[17] A. Inoue, F.L. Kong, Y. Han, *et al.*, Development and application of Fe-based soft magnetic bulk metallic glassy inductors, *J. Alloy. Compd.*, 731(2018), p. 1303.

[18] X. Li, Y. Liu, D.C. Yu, *et al.*, Effect of Cr addition on glass-forming ability and corrosion properties of FeCoSiBPC bulk glassy alloys, *Mater. Trans.*, 59(2018), No. 8, p. 1375.

[19] S. Sharma and C. Suryanarayana, Effect of Nb on the glass-forming ability of mechanically alloyed Fe–Ni–Zr–B alloys, *Scripta Mater.*, 58(2008), No. 6, p. 508.

[20] A. Guinier, *X-ray Diffraction in Crystals, Imperfect Crystals and Amorphous Bodies*, W.H. Freeman and company, San Francisco, 1963, p. 72.

[21] H.E. Kissinger, Reaction kinetics in differential thermal analysis, *Anal. Chem.*, 29(1957), No.11, p. 1702.

[22] Y. Wang, Y.Z. Wang, J.F. Wang, J. Wang, and Z. Zheng, Crystallization behavior of $Ce_{70-x}Al_{10}Cu_{20}Co_x$ (x = 0, 1, 3, 5 at.%) amorphous alloys, *J. Non-Cryst. Solids*, 358(2012), No. 15, p. 1735.

[23] A.H. Taghvaei, R. Farajollahi, J. Bednarčík, J. Eckert, and M. Pahlevani, Atomic structure, thermal stability and isothermal crystallization kinetics of novel Co-based metallic glasses with excellent soft magnetic properties, *J. Alloy. Compd.*, 963(2023), art. No. 171271.

[24] T. Bitoh, A. Makino, and A. Inoue, Origin of low coercivity of $(Fe_{0.75}B_{0.15}Si_{0.10})_{100-x}Nb_x$ (x = 1–4) glassy alloys, *J. Appl. Phys.*, 99(2006), No. 8, art. No. 08F102.

[25] H. Kronmüller, M. Fähnle, M. Domann, H. Grimm, R. Grimm, and B. Gröger, Magnetic properties of amorphous ferromagnetic alloys, *J. Magn. Magn. Mater.*, 13(1979), No. 1-2, p. 53.

[26] H. Kronmüller, Micromagnetism and microstructure of amorphous alloys (invited), *J. Appl. Phys.*, 52(1981), No. 3, p. 1859.

[27] S. Lan, L. Zhu, Z.D. Wu, *et al.*, A medium-range structure motif linking amorphous and crystalline states, *Nat. Mater.*, 20(2021), No. 10, p. 1347.

[28] H. Zhang, Z. Wang, P.K. Liaw, and J.W. Qiao, A criterion of the critical threshold of the maximum shear stress in bulk metallic glasses with cryogenic thermal cycling by statistics in nanoindentation, *Mater. Sci. Eng. A*, 873(2023), art. No. 145031.

[29] G.Q. Liu, Z.Q. Xiao, N.R. Wang, *et al.*, Synthesis and characterization of soft-magnetic $(Fe_{0.7}Co_{0.3})_{75}B_{21}Ta_4$ metallic glasses by annealing and cryogenic treatment, *J. Non-Cryst. Solids*, 581(2022), art. No. 121411.

[30] S.C. Zhai, Z.R. Peng, Y.F. Guan, Z. Ding, W. Wang, and Y. Wang, Soft magnetic properties and corrosion resistance of Fe–Co–B–M (M = Nb, Ta and NbNi) metallic glasses, *J. Non-Cryst. Solids*, 506(2019), p. 28.

[31] S.C. Zhai, *Microstructure, Thermal Stability and Corrrosion Resistance of Soft Magnetic Fe-based Amorphous Alloys* [Dissertaion], University of Jinan, Jinan, 2019, p. 23.

[32] H. Kronmüller, Theory of the coercive field in amorphous ferromagnetic alloys, *J. Magn. Magn. Mater.*, 24(1981), No. 2, p. 159.

[33] J.J. Han, C.P. Wang, S.Z. Kou, and X.J. Liu, Thermal stability, crystallization behavior, Vickers hardness and magnetic properties of Fe–Co–Ni–Cr–Mo–C–B–Y bulk metallic glasses, *Trans. Nonferrous Met. Soc. China*, 23(2013), No. 1, p. 148.

[34] A.H. Taghvaei, M. Stoica, K.G. Prashanth, and J. Eckert, Fabrication and characterization of bulk glassy $Co_{40}Fe_{22}Ta_8B_{30}$ alloy with high thermal stability and excellent soft magnetic properties, *Acta Mater.*, 61(2013), No. 17, p. 6609.

[35] Z.N. Wang, Y. Yan, Y. Wu, *et al.*, Corrosion and tribocorrosion behavior of equiatomic refractory medium entropy TiZr (Hf, Ta, Nb) alloys in chloride solutions, *Corros. Sci.*, 199(2022), art. No. 110166.

[36] C. Nyby, X.L. Guo, J.E. Saal, *et al.*, Electrochemical metrics for corrosion resistant alloys, *Sci. Data*, 8(2021), No. 1, art. No. 58.

[37] C.L. Zhu, Q. Wang, J. Zhang, Y.M. Wang, and C. Dong, Formation and corrosion properties of Fe-based bulk metallic glasses, *Int. J. Miner. Metall. Mater.*, 17(2010), No. 3, p. 323.

[38] M.K. Tam, S.J. Pang, and C.H. Shek, Effects of niobium on thermal stability and corrosion behavior of glassy Cu–Zr–Al–Nb alloys, *J. Phys. Chem. Solids*, 67(2006), No. 4, p. 762.

[39] C. Poddar, S. Ningshen, and J. Jayaraj, Corrosion assessment of $Ni_{60}Nb_{30}Ta_{10}$ metallic glass and its partially crystallized alloy in concentrated nitric acid environment, *J. Alloy. Compd.*, 813(2020), art. No. 152172.

[40] Z.M. Wang, J. Zhang, X.C. Chang, W.L. Hou, and J.Q. Wang, Structure inhibited pit initiation in a Ni–Nb metallic glass, *Corros. Sci.*, 52(2010), No. 4, p. 1342.